Spin-carrier coupling induced ferromagnetism and giant resistivity peak in math xmlns="http://www.w3.org/1998/Math/MathML">msub>mi mathvariant="normal">EuCd/mi>mn>2/mn>/msub>msub >mi mathvariant="normal">P/mi>mn>2/mn> /msub>/math>

V. Sunko, Y. Sun, M. Vranas, C. C. Homes, C. Lee, E. Donoway, Z.-C. Wang, S. Balguri, M. B. Mahendru, A. Ruiz, B. Gunn, R. Basak, S. Blanco-Canosa, E. Schierle, E. Weschke, F. Tafti, A. Frano, and J. Orenstein

Phys. Rev. B **107**, 144404 — Published 4 April 2023

DOI: 10.1103/PhysRevB.107.144404

Spin-carrier coupling induced ferromagnetism and giant resistivity peak in $EuCd_2P_2$

V. Sunko,[1,2,*] Y. Sun,[1,2,*] M. Vranas,[3] C. C. Homes,[4] C. Lee,[2] E. Donoway,[2] Z.-C. Wang,[5] S. Balguri,[5] M. B. Mahendru,[5] A. Ruiz,[3] B. Gunn,[3] R. Basak,[3] S. Blanco-Canosa,[6,7] E. Schierle,[8] E. Weschke,[8] F. Tafti,[5] A. Frano,[3] and J. Orenstein[1,2]

[1]*Department of Physics, University of California, Berkeley, California 94720, USA*
[2]*Materials Science Division, Lawrence Berkeley National Laboratory, Berkeley, California 94720, USA*
[3]*Department of Physics, University of California, San Diego, California 92093, USA*
[4]*NSLS II, Brookhaven National Laboratory, Upton, New York 11973, USA*
[5]*Department of Physics, Boston College, Chestnut Hill, Massachusetts 02467, USA*
[6]*Donostia International Physics Center, DIPC, 20018 Donostia-San Sebastian, Basque Country, Spain*
[7]*IKERBASQUE, Basque Foundation for Science, 48013 Bilbao, Spain*
[8]*Helmholtz-Zentrum Berlin fr Materialien und Energie, Albert-Einstein-Strae 15, 12489 Berlin, Germany*

$EuCd_2P_2$ is notable for its unconventional transport: upon cooling the metallic resistivity changes slope and begins to increase, ultimately 100-fold, before returning to its metallic value. Surprisingly, this giant peak occurs at 18 K, well above the Néel temperature (T_N) of 11.5 K. Using a suite of sensitive probes of magnetism, including resonant x-ray scattering and magneto-optical polarimetry, we have discovered that ferromagnetic order onsets above T_N in the temperature range of the resistivity peak. The observation of inverted hysteresis in this regime shows that ferromagnetism is promoted by coupling of localized spins and itinerant carriers. The resulting carrier localization is confirmed by optical conductivity measurements.

First glimpses of phase transitions in new materials are often gained through measurement of the temperature-dependent resistivity, $\rho(T)$. At a magnetic transition $\rho(T)$ of a metal generically exhibits a change in slope, with $d\rho/dT$ proportional to the heat capacity anomaly. This behavior is understood within the Fisher-Langer theory, in which enhanced quasiparticle scattering appears as a consequence of critical fluctuations [1]. However, some metallic magnets exhibit features in $\rho(T)$ more pronounced than a mere change in slope. For example, resistivity peaks have been reported recently near the Néel temperature T_N in a number of antiferromagnetic (AFM) europium compounds with the general formula EuM_2C_2 (M=In,Cd, C=Sb, As, P) [2–7]. In these materials magnetism is localized in Eu^{2+} layers, which are separated by low-carrier density itinerant M_2C_2 blocks. They are notable because density-functional theory predicts that their low-energy electronic structure and topology are dramatically altered by the nature of the magnetic order [8–15], and that the different magnetic states are close in energy [16], and are therefore experimentally accessible [2, 17–19]. This combination offers the exciting prospect of creating electronic states hypersensitive to external stimuli.

The resistivity of $EuCd_2P_2$, the subject of this study (see Sec. I of the Supplementary Information [20] for sample preparation ans characterization, stands out as an extreme example of unconventional temperature dependence, quantitatively and qualitatively different from other systems exhibiting a resistivity peak [5]. As shown in Fig. 1, the metallic high-temperature resistivity (green in Fig. 1c) undergoes a hundredfold increase with decreasing temperature (blue) and subsequently returns to metallic values (purple). Both the rise and fall of the resistance take place well above the Néel temperature of 11.5 K, as determined from the heat capacity measurements. The peak value of ρ, which is found at 18 K, is suppressed by modest magnetic fields, yielding a giant negative magnetoresistance [5].

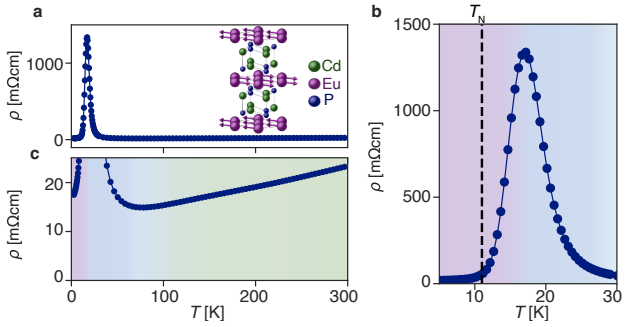

Figure 1. (a,b) The resistivity of $EuCd_2P_2$ (structure in the inset) shows a pronounced peak at 18 K. (c) Above 75 K it exhibits metallic behavior. Data are from Ref. [5].

Here we use a powerful combination of bespoke magneto-optical techniques and x-ray scattering to show that the anomalous resistivity peak does not arise due to antiferromagnetism, but it is a consequence of a previously unreported time-reversal breaking that takes place above the Néel temperature. Our results indicate that AFM order is preceded by the formation of ferromagnetic clusters driven by the interaction of localized spin and itinerant charge degrees of freedom. The three resistivity regimes depicted in Fig. 1 are traced to temperature-dependent crossovers from independent fluctuating clusters to the onset of ferromagnetic order.

We begin by describing our spatially-resolved symmetry-sensitive optical measurements, in which we measure the change of the angle of linear polarization ($d\phi$) as a function of sample orientation. Since we cannot physically rotate the sample fixed to piezoelectric scanning stages, we access the same information by rotating the incoming light polarization (ϕ). Once the experimental setup is carefully aligned to preserve the polarization state (SI, Sec. III), the change of polarization upon reflection is given by:

$$d\phi \sim A\,(T)\sin\left[2\left(\phi-\phi_0\,(T)\right)\right]+B\,(T)\,, \qquad (1)$$

where $\phi_0\,(T)$ and $\phi_0\,(T)+\pi/2$ indicate the directions of the principal optical axes, and $A\,(T)$ and $B\,(T)$ are proportional to birefringence and polar magneto-optical Kerr effect (pMOKE). These effects arise from the breaking of rotational symmetry and out-of-plane magnetization, M_z, respectively. To enhance experimental sensitivity, we modulate T at a frequency $f \approx 2\,\mathrm{kHz}$ using a second laser beam as a heater, essentially measuring the temperature derivatives of A and B, dA and dB [21, 22].

This experiment at 2 K reveals a sinusoidal dependence of $d\phi$ on ϕ (Fig. 2a, Eq. 1), corresponding to a nonzero value of dA and indicating broken rotational symmetry. Fig. 2b is a map of the spatial distribution of ϕ_0, revealing three birefringent domains with 120 ° between their principal axes (see Fig. S2a of SI for histogram of the relative domain populations). This observation is consistent with spontaneous breaking of C_3 symmetry at the onset of previously reported type A-AFM order (i.e., alternating ferromagnetic layers with in-plane spins, ref. [5]) on a triangular lattice.

The first indication of unconventional order in $EuCd_2P_2$ is the observation of nonzero dB, indicated by the ϕ-independent offset of the sinusoidal curves in Fig. 2b. As mentioned above, this offset demonstrates the existence of an out-of-plane component of magnetization, M_z; we therefore refer to it as dM_z for clarity. The dM_z map (Fig. 2c) shows that domains of M_z and A-AFM order are highly correlated, suggesting coexistence and strong coupling between the two forms of order. In contrast, reflectivity is uniform across this sample region (see Figs. S1(b-d)).

The temperature dependence of dA shown in Fig. 2d exhibits an additional surprising feature: the birefringence that was provisionally attributed to antiferromagnetism does not vanish at T_N. Rather, with increasing temperature there is a discontinuous change in slope at T_N followed by a gradual decrease in amplitude, showing that C_3 symmetry remains broken above T_N. dM_z also remains nonzero above T_N, with the polar Kerr signal changing smoothly through the transition. We emphasize that both of these signals indicate static order, and cannot arise due to fluctuations. Zooming in on the weak feature at $\sim 2T_N$, we see peaks in both temperature-modulated birefringence and pMOKE (Fig. 2d, inset).

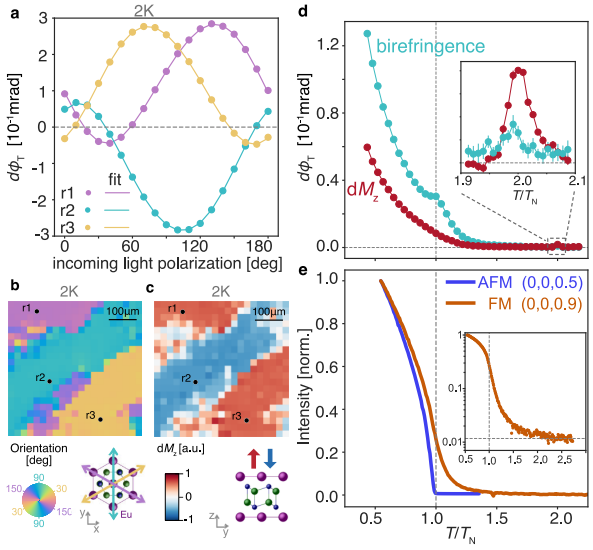

Figure 2. (a) Thermally-modulated polarization rotation as a function of incident polarization and corresponding fits (Eq. 1), measured at three sample locations (probe: 20 μW, 633 nm; pump: 50 μW, 780 nm, modulated at 2345 Hz). (b, c) Maps of (b) principal axis orientation and (c) dM_z, extracted from the phase and offset of curves like those in (a) (step size: 25 μm, light spot diameter: 5 μm). (d) Thermally-modulated birefringence amplitude (teal) and dM_z (red) as a function of temperature ($T_N = 11.5\,\mathrm{K}$). Both signals onset at $\sim 2T_N$ (inset). (e)Normalized antiferromagnetic (blue; $(h,k,l) = (0,0,0.5)$) and ferromagnetic (orange; $(h,k,l) = (0,0,0.9)$, with structural scattering subtracted) REXS as a function of temperature. AFM scattering onsets sharply at T_N, in contrast to the gradual onset of ferromagnetism around $2T_N$, emphasized in the logarithmic plot in the inset.

Since the temperature-modulated measurements are sensitive to the temperature derivatives of birefringence and pMOKE, the peaks in the inset correspond to the onsets of the two order parameters. The simultaneous onsets indicate that the order parameters are likely coupled.

To help identify the origin of rotational symmetry breaking above T_N, we employed resonant elastic x-ray scattering (REXS), with photon energy tuned to the Eu M_5 edge (1127.5 eV). The amplitude of the (0 0 0.5) diffraction peak, corresponding to A-AFM order, drops sharply at $T_N = 11.5\,\mathrm{K}$, ruling out A-AFM order as the source of C_3 breaking above T_N (Fig. 2e). The ferromagnetic (FM) peak at (0 0 1) is obscured by the structural one; however a fortunate matrix element suppression of the structural Thomson scattering at (0 0 0.9) provides a window to the FM order (for details see SI, Sec. IV). In contrast with the AFM onset, the FM order decreases smoothly through T_N (Fig. 2f), mirroring the $dM_z(T)$ extracted from the pMOKE signal (Fig. 2d), and can be traced up to $\sim 2T_N$ (inset). We note that our measurements indicate static FM order, in contrast to short-range fluctuations reported in the sibling compound $EuCd_2As_2$ [23].

Having confirmed the existence of ferromagnetic order for $T > T_N$, we turn to the origin of rotational symmetry breaking above the Néel temperature. In particular, we explore the idea that the rotational symmetry breaking is caused by an in-plane component of magnetization, $M_{||}$. While in principle $M_{||}$ can be detected by thermally-modulated longitudinal and transverse Kerr effect [22] measured at a finite incidence angle, the large birefringence observed at normal incidence would hinder such experiments. We have therefore developed a new method, based on the linear magneto-optic effect [24–31], to isolate rotational symmetry breaking associated with order parameters that break time-reversal symmetry, as well. Specifically, we measure the modulation of birefringence that is linear in an applied magnetic field; we refer to this effect as linear magneto-birefringence (LMB), and parameterize it by the LMB tensor,

$$\overleftrightarrow{\delta r} = \begin{pmatrix} \beta & \gamma \\ \gamma & -\beta \end{pmatrix} H_z, \qquad (2)$$

where $\overleftrightarrow{\delta r}$ is the change of reflectance, H_z is an applied field, and $(1,0)$ and $(0,1)$ correspond to the principal axes at $H_z = 0$. As a consequence of Onsager's relation, the LMB tensor vanishes in time-reversal (TR) invariant systems (see SI, Sec. V for a derivation), making it a sensitive probe of TR symmetry breaking.

We measure the components of $\overleftrightarrow{\delta r}$ by detecting the change in reflectivity at the fundamental frequency of an oscillating H_z, applied by a small coil [32]. After careful calibration of the setup (SI, Sec. III.C), the change in polarization on reflection that is synchronous with the applied field, $d\phi \sim AH_z \sin[2(\phi + \phi_C)]$, yields the elements of the LMB tensor through the relations,

$$A^2 = \beta^2 + \gamma^2, \quad \phi_C = \phi_0 + \frac{1}{2}\arctan\frac{\gamma}{\beta}, \qquad (3)$$

where ϕ_0 is the principal axes orientation at $H_z = 0$.

Fig. 3a shows the existence of LMB in $EuCd_2P_2$ at 16 K. The diamonds and circles compare the change in polarization induced by field and temperature modulation, respectively, and demonstrate a phase shift of 52 ° between them. The observation of a phase shift that is not equal to either 0 ° or 45 ° proves that both β and γ are nonzero (Eq. 3). A symmetry analysis of the LMB tensor in $EuCd_2P_2$, summarized in Fig. 3b and discussed in detail in Sec. V of SI, shows that the only component of magnetization which can induce a nonzero γ is M_y, revealing this component of FM order above T_N, and identifying it as the origin of birefringence above the AFM transition.

The temperature dependence of the field-modulated amplitude, plotted in Fig. 3c, shows that LMB vanishes at $\sim 2T_N$, coincident with the disappearance of M_z (Fig. 2d), and the ferromagnetic REXS scattering (Fig. 2e). Although the onset temperature of the LMB

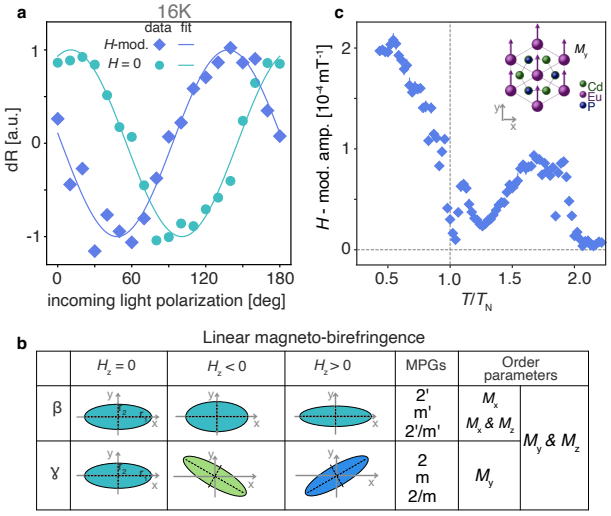

Figure 3. (a) The phase difference between the H_z-linear birefringence (diamonds) and the $H = 0$ birefringence (circles) proves $\gamma \neq 0$ (Eq. 3), and therefore $M_y \neq 0$ (inset of (c)). For clarity the curves are normalized by the respective amplitudes, and constant offsets are subtracted. (b) Diagonal (β) and off-diagonal (γ) LMB: the orientation and length of the ellipse axes represent the orientation of the optic principal axes and the reflectivity along them, respectively. Magnetic point groups (MPGs) and order parameters compatible with the two effects are listed. (c) The amplitude of LMB as a function of temperature ($T_N = 11.5$ K) reveals the onset of TR - and C_3- broken phase at $\sim 2T_N$. Probe beam: 20 μW, 633 nm; field amplitude: 0.2 mT, modulated at 500 Hz.

signal is reproducible, the details of the LMB amplitude as a function of temperature in the ferromagnetic state depend on the specific domain configuration, which changes on each cooldown (Section VI of the SI), as expected of a state which spontaneously breaks time reversal symmetry.

We have now provided three complementary pieces of evidence for the onset of static ferromagnetism in $EuCd_2P_2$: pMOKE and LMB, which are directly sensitive to time-reversal symmetry breaking, confirm the presence of M_z and M_y, respectively, while the elemental specificity and momentum resolution of REXS unambiguously identify Eu atoms in $EuCd_2P_2$ as the source of the ferromagnetism. Motivated by these results, we repeated bulk magnetization measurements, first reported in Ref. [5], on a larger sample to ensure better signal to noise ratio, and we were indeed able to observe a small hysteretic moment of 0.01 μ_B at 3 K, setting a lower bound on the ferromagnetic volume fraction to 0.1% (see Section VIII of SI for the analysis).

We note that M_y and M_z correspond to distinct magnetic point groups, so one is not a natural consequence of the other, as in 'weak ferromagnetism' [33], for example. Their coexistence indicates coupling via a high-order magnetocrystalline anisotropy (MCA), which typi-

cally arises from a combination of spin-orbit coupling and the crystal field [34]. However, the ground state of Eu^{2+} carries no angular momentum [35], so spin-orbit coupling is expected to be negligible and the anisotropy cannot be understood by considering only Eu spins. Instead, the MCA can stem from the coupling of Eu to carriers, as was previously demonstrated in other magnets containing the $L = 0$ Eu^{2+} or Gd^{3+} ions [36–38].

Confirmation that ferromagnetism in $EuCd_2P_2$ results from the coupling between Eu spins and conduction electrons comes from measurements of dM_z as a function of applied dc magnetic field. Fig. 4a follows the magnetization through a field sweep at 3 K, showing a hysteresis loop that confirms FM order. The same field sweep conducted at 14 K (Fig. 4b) is also hysteretic, but looks very different in two respects: the loop proceeds clockwise rather than counterclockwise, and is superposed on a linear background. Removing the background (inset) emphasizes the hysteresis is *inverted*: the saturated magnetization is anti-parallel to the applied field direction!

Inverted hysteresis cannot arise from a single class of ferromagnetically coupled spins; instead, at least two *antiferromagnetically* coupled subsystems are required. A minimum model for the observed behavior is described by the free energy,

$$F = \alpha_2 m^2 + \beta_2 M^2 + \beta_4 M^4 + JmM - H(m + M), \quad (4)$$

where m and M are the magnetization of carriers and Eu ions, respectively, J is the antiferromagnetic coupling between them, and the parameters α_n and β_n are the quadratic and quartic terms in the expansion in even powers of the magnetization. With $H = 0$, F has a minimum at nonzero magnetization,

$$M^2 = \frac{1}{4\beta_4}\left(\frac{J^2}{2\alpha_2} - 2\beta_2\right), \quad m = -\frac{J}{2\alpha_2}M, \qquad (5)$$

for coupling strengths $J^2 > 4\beta_2\alpha_2$, showing that J promotes spontaneous magnetization, even if the uncoupled Eu system would be paramagnetic ($\beta_2 > 0$).

Minimizing the free energy with $H \neq 0$ yields (SI, Sec. VII):

$$M^3 - \frac{M}{4\beta_4}\left(\frac{J^2}{2\alpha_2} - 2\beta_2\right) - \frac{H}{4\beta_4}\left(1 - \frac{J}{2\alpha_2}\right) = 0. \quad (6)$$

Eq. 6 suggests that the effective magnetic field experienced by the Eu spin is opposite in sign to the applied field if J is larger than $2\alpha_2$, yielding the inverted Eu hysteresis. Although the total magnetization, $M + m$, is parallel to the applied field, our experiment is dominantly sensitive to Eu magnetization, and therefore capable of observing its inverted hysteresis. The existence of both normal and inverted Eu hysteresis within this model is demonstrated in Figs. 4(c, d), which illustrate M vs. H for $J < 2\alpha_2$ and $J > 2\alpha_2$, respectively. Both regimes

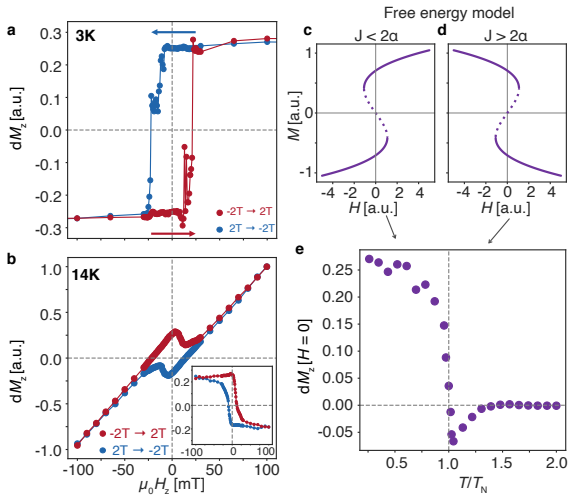

Figure 4. dM_z as a function of H_z for increasing (red) and decreasing (blue) field at (a) 3 K and (b) 14 K, revealing the opposite sense of hysteresis at the two temperatures. Removing the linear background in (b) shows the inverted hysteresis (inset). (c,d) The real solutions of Eq. 6, for (c) $J < 2\alpha$ and (d) $J > 2\alpha$. The full and dotted lines correspond to local minima and saddle points of the free energy, respectively. (e) The temperature dependence of the magnetization at zero field, defined as half the difference between the dM_z ($H = 0$), measured while increasing and decreasing the field.

exhibit classic bistable behavior, with three solutions for $\partial F/\partial M = \partial F/\partial m = 0$ at low applied field; two stable minima (solid lines) and one saddle point (dashed line). Mirrored trajectories of M vs. H_z in Figs. 4(c, d) correspond to normal and inverted hysteresis, respectively.

The temperature dependence of the zero-field magnetization (Fig. 4e), defined to be positive for normal hysteresis, shows that the transition from normal to inverted regimes occurs at T_N. The onset of the antiferromagnetic order therefore disrupts the delicate balance required for realization of the inverted hysteresis. Our model suggests that this is caused by a reduction in the effective spin-carrier interaction, J/α_2, as expected from the decrease in the spin-polarization of the electrons due to their coupling to the AFM order.

These observations of a bulk FM order, and the inverted hysteresis above T_N, offer compelling evidence for the role of spin-carrier coupling in determining the magnetic properties of $EuCd_2P_2$. We now turn to the role of this coupling in its remarkable resistivity. To help address this question we augmented our magneto-optical and x-ray probes with measurements of the frequency- and temperature- dependent conductivity, $\sigma_1(\omega, T)$, obtained by Kramers-Kronig analysis of broadband reflectivity.

Fig. 5a shows optical conductivity spectra measured at the resistivity peak (18 K), together with representative spectra measured in the metallic regime at temperatures above (50 K) and below (5 K). The contrast in the

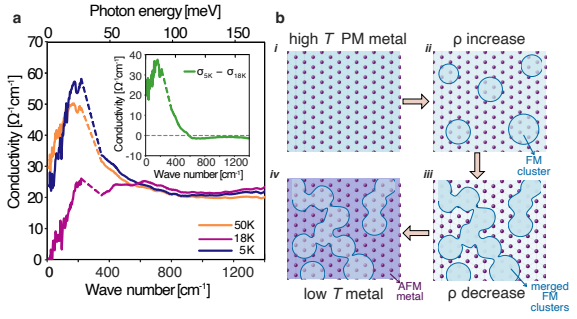

Figure 5. (a) Optical conductivity at 50 K, 18 K and 5 K, showing electron localization at 18 K. The inset is the difference between the 5 K and the 18 K data, showing the conduction electron spectral weight. The dashed lines are interpolations across a region where the measurement is dominated by the spectral weight of an optical phonon. (b) Schematic temperature evolution of the coupled Eu-electron system.

spectra between the high and low conductivity regimes provides a clear picture of the dynamics that underline the giant resistance peak. While the optical conductivity at 5 K and 50 K is remarkably similar, $\sigma_1(\omega, 18\,\mathrm{K})$ is clearly suppressed at low frequencies. Subtracting the spectrum measured at 18 K from that measured at 5 K reveals a Drude-like peak (Fig. 5a, inset). We attribute the metallic conductivity observed in the high and low temperature regimes to this component of $\sigma_1(\omega)$; the resistivity peak at 18 K then reflects its vanishing. We note that standard analysis of the optical conductivity and Hall effect (SI, Sec. IX.) yields a carrier concentration $n_e = 0.6 \times 10^{19}\,\mathrm{cm}^{-3}$, scattering rate $\Gamma = 9 \times 10^{13}\mathrm{s}^{-1}$, and a mass of $1.5m_e$, where m_e is the free electron mass. The conductivity spectra measured as T passes through the peak in resistivity confirm that the increase in ρ originates from a dramatic decrease in n_e rather than an increase in Γ (Fig. 5a, and ref. [39]). Optical conductivity therefore offers unambiguous evidence of electron localization.

While non-monotonic temperature dependence of resistivity in *non-magnetic* f-electron metals is typically attributed to Kondo scattering (see ref. [35] for discussion in Eu-compounds), a unifying theoretical explanation for resistivity peaks in metallic magnets is lacking [40–43]. $EuCd_2P_2$ is an outlier in both the giant amplitude and location in temperature of the maximum in $\rho(T)$. Nonetheless, our combination of optical polarimetry, x-ray, and far-infrared measurements points to spontaneous phase separation, similar to that observed in the *ferromagnetic* metal EuB_6 [44–46]. In this scenario (Fig. 5b) high-temperature metallic behavior is interrupted by phase separation: electrons localize into spin-polarized clusters, within which spins align due to the spin-carrier coupling (J in Eq. 4). The localization (Fig. 5a) causes the resistivity to increase with decreasing temperature, starting at $\sim$ 75 K. The increase of resistivity is slowed down as percolating conducting paths start to form, eventually causing the resistivity to decrease. The width of the resistivity peak is therefore determined by the combination of two processes: ferromagnetic cluster formation and percolation. The percolation picture also helps explain the colossal magnetoresistance reported in Ref. [5]: an externally applied magnetic field promotes growth of the ferromagnetic clusters, and therefore percolation, limiting the increase of resistivity in the peak region. The merged clusters develop a net ferromagnetic moment (M_y, M_z), detected by our suite of probes (REXS, pMOKE and LMB). In particular, the spontaneous phase separation is seen in the behavior of the magnetization vs. H_z in this regime (Fig. 4b): paramagnetic Eu spins contribute the linear background, while the inverted hysteresis arises in the carrier-mediated ferromagnetic regions.

Our finding that the same process, i.e. the spontaneous formation and percolation of ferromagnetic clusters, is responsible for resistivity in both $EuCd_2P_2$ and EuB_6, is surprising. The two compounds exhibit different magnetic order, and drastically different resistivity anomalies: the 100-fold increase of ρ in the AFM $EuCd_2P_2$ *versus* the 20% increase in the FM EuB_6. We suggest that the low carrier density and the frustration resulting from near degeneracy of ferro- and antiferromagnetic states in $EuCd_2P_2$ are the key ingredients yielding the enhanced effect. These ingredients are then principles that can guide the design of other systems in which transport displays hypersensitivity to external control parameters such as temperature and electromagnetic fields. Furthermore, our work motivates future experiments to directly visualize the ferromagnetic clusters, as well as the development of a unified theoretical description of resistivity in a wide range of systems with strong carrier-spin interactions, and offers ways to experimentally constrain such models.

We thank Elbio Dagotto, Andrew Mackenzie, Chunxiao Liu, Marc Vila Tusell, Thomas Scaffidi and Ehud Altman for useful discussions. Optical measurements were performed at the Lawrence Berkeley Laboratory as part of the Quantum Materials program, Director, Office of Science, Office of Basic Energy Sciences, Materials Sciences and Engineering Division, of the U.S. Department of Energy under Contract No. DE-AC02-05CH11231. V.S. is supported by the Miller Institute for Basic Research in Science, UC Berkeley. J.O and Y.S received support from the Gordon and Betty Moore Foundation's EPiQS Initiative through Grant GBMF4537 to J.O. at UC Berkeley. F. T. and S. B. acknowledge funding from the Schiller Institute Grant for Exploratory Collaborative Scholarship (SIGECS). Work at Brookhaven National Laboratory was supported by the Office of Science, U.S. Department of Energy under Contract No. DE-SC0012704. This material is based upon work supported by the National Science Foundation under Grant No. DMR-2145080.

* V. S. and Y. S. contributed equally to this work.

[1] M. E. Fisher and J. S. Langer, Resistive Anomalies at Magnetic Critical Points, Physical Review Letters **20**, 665 (1968).

[2] J.-Z. Ma, S. M. Nie, C. J. Yi, J. Jandke, T. Shang, M. Y. Yao, M. Naamneh, L. Q. Yan, Y. Sun, A. Chikina, V. N. Strocov, M. Medarde, M. Song, Y.-M. Xiong, G. Xu, W. Wulfhekel, J. Mesot, M. Reticcioli, C. Franchini, C. Mudry, M. Müller, Y. G. Shi, T. Qian, H. Ding, and M. Shi, Spin fluctuation induced Weyl semimetal state in the paramagnetic phase of $EuCd_2As_2$, Science Advances **5**, eaaw4718 (2019).

[3] Y. Xu, L. Das, J. Z. Ma, C. J. Yi, S. M. Nie, Y. G. Shi, A. Tiwari, S. S. Tsirkin, T. Neupert, M. Medarde, M. Shi, J. Chang, and T. Shang, Unconventional Transverse Transport above and below the Magnetic Transition Temperature in Weyl Semimetal $EuCd_2As_2$, Physical Review Letters **126**, 076602 (2021).

[4] M. C. Rahn, J.-R. Soh, S. Francoual, L. S. I. Veiga, J. Strempfer, J. Mardegan, D. Y. Yan, Y. F. Guo, Y. G. Shi, and A. T. Boothroyd, Coupling of magnetic order and charge transport in the candidate Dirac semimetal $EuCd_2As_2$, Physical Review B **97**, 214422 (2018).

[5] Z.-C. Wang, J. D. Rogers, X. Yao, R. Nichols, K. Atay, B. Xu, J. Franklin, I. Sochnikov, P. J. Ryan, D. Haskel, and F. Tafti, Colossal Magnetoresistance without Mixed Valence in a Layered Phosphide Crystal, Advanced Materials **33**, 2005755 (2021).

[6] H. Su, B. Gong, W. Shi, H. Yang, H. Wang, W. Xia, Z. Yu, P.-J. Guo, J. Wang, L. Ding, L. Xu, X. Li, X. Wang, Z. Zou, N. Yu, Z. Zhu, Y. Chen, Z. Liu, K. Liu, G. Li, and Y. Guo, Magnetic exchange induced Weyl state in a semimetal $EuCd_2Sb_2$, APL Materials **8**, 011109 (2020).

[7] Y. Zhang, K. Deng, X. Zhang, M. Wang, Y. Wang, C. Liu, J.-W. Mei, S. Kumar, E. F. Schwier, K. Shimada, C. Chen, and B. Shen, In-plane antiferromagnetic moments and magnetic polaron in the axion topological insulator candidate $EuIn_2As_2$, Physical Review B **101**, 205126 (2020).

[8] Y. Xu, Z. Song, Z. Wang, H. Weng, and X. Dai, Higher-Order Topology of the Axion Insulator $EuIn_2As_2$, Physical Review Letters **122**, 256402 (2019).

[9] G. Hua, S. Nie, Z. Song, R. Yu, G. Xu, and K. Yao, Dirac semimetal in type-IV magnetic space groups, Physical Review B **98**, 201116 (2018).

[10] J.-R. Soh, F. de Juan, M. G. Vergniory, N. B. M. Schröter, M. C. Rahn, D. Y. Yan, J. Jiang, M. Bristow, P. Reiss, J. N. Blandy, Y. F. Guo, Y. G. Shi, T. K. Kim, A. McCollam, S. H. Simon, Y. Chen, A. I. Coldea, and A. T. Boothroyd, Ideal Weyl semimetal induced by magnetic exchange, Physical Review B **100**, 201102 (2019).

[11] L.-L. Wang, N. H. Jo, B. Kuthanazhi, Y. Wu, R. J. McQueeney, A. Kaminski, and P. C. Canfield, Single pair of Weyl fermions in the half-metallic semimetal $EuCd_2As_2$, Physical Review B **99**, 245147 (2019).

[12] J.-R. Soh, C. Donnerer, K. M. Hughes, E. Schierle, E. Weschke, D. Prabhakaran, and A. T. Boothroyd, Magnetic and electronic structure of the layered rare-earth pnictide $EuCd_2Sb_2$, Physical Review B **98**, 064419 (2018).

[13] X. Gui, I. Pletikosic, H. Cao, H.-J. Tien, X. Xu, R. Zhong, G. Wang, T.-R. Chang, S. Jia, T. Valla, W. Xie, and R. J. Cava, A New Magnetic Topological Quantum Material Candidate by Design, ACS Central Science **5**, 900 (2019).

[14] S. X. M. Riberolles, T. V. Trevisan, B. Kuthanazhi, T. W. Heitmann, F. Ye, D. C. Johnston, S. L. Bud'ko, D. H. Ryan, P. C. Canfield, A. Kreyssig, A. Vishwanath, R. J. McQueeney, L.-L. Wang, P. P. Orth, and B. G. Ueland, Magnetic crystalline-symmetry-protected axion electrodynamics and field-tunable unpinned Dirac cones in $EuIn_2As_2$, Nature Communications **12**, 999 (2021).

[15] K. M. Taddei, L. Yin, L. D. Sanjeewa, Y. Li, J. Xing, C. dela Cruz, D. Phelan, A. S. Sefat, and D. Parker, Single pair of Weyl nodes in the spin-canted structure of $EuCd_2As_2$, Physical Review B **105**, L140401 (2022).

[16] J. Krishna, T. Nautiyal, and T. Maitra, First-principles study of electronic structure, transport, and optical properties of $EuCd_2As_2$, Physical Review B **98**, 125110 (2018).

[17] N. H. Jo, B. Kuthanazhi, Y. Wu, E. Timmons, T.-H. Kim, L. Zhou, L.-L. Wang, B. G. Ueland, A. Palasyuk, D. H. Ryan, R. J. McQueeney, K. Lee, B. Schrunk, A. A. Burkov, R. Prozorov, S. L. Bud'ko, A. Kaminski, and P. C. Canfield, Manipulating magnetism in the topological semimetal $EuCd_2As_2$, Physical Review B **101**, 140402 (2020).

[18] N. H. Jo, Y. Wu, T. V. Trevisan, L.-L. Wang, K. Lee, B. Kuthanazhi, B. Schrunk, S. L. Bud'ko, P. C. Canfield, P. P. Orth, and A. Kaminski, Visualizing band selective enhancement of quasiparticle lifetime in a metallic ferromagnet, Nature Communications **12**, 7169 (2021).

[19] E. Gati, S. L. Bud'ko, L.-L. Wang, A. Valadkhani, R. Gupta, B. Kuthanazhi, L. Xiang, J. M. Wilde, A. Sapkota, Z. Guguchia, R. Khasanov, R. Valentí, and P. C. Canfield, Pressure-induced ferromagnetism in the topological semimetal $EuCd_2As_2$, Physical Review B **104**, 155124 (2021).

[20] See supplemental material at [url will be inserted by publisher], for additional information.

[21] A. Little, C. Lee, C. John, S. Doyle, E. Maniv, N. L. Nair, W. Chen, D. Rees, J. W. F. Venderbos, R. M. Fernandes, J. G. Analytis, and J. Orenstein, Three-state nematicity in the triangular lattice antiferromagnet $Fe_{1/3}NbS_2$, Nature Materials **19**, 1062 (2020).

[22] Y. Sun, C. Lee, H.-Y. Yang, D. H. Torchinsky, F. Tafti, and J. Orenstein, Mapping domain-wall topology in the magnetic Weyl semimetal CeAlSi, Physical Review B **104**, 235119 (2021).

[23] J.-R. Soh, E. Schierle, D. Y. Yan, H. Su, D. Prabhakaran, E. Weschke, Y. F. Guo, Y. G. Shi, and A. T. Boothroyd, Resonant x-ray scattering study of diffuse magnetic scattering from the topological semimetals $EuCd_2As_2$ and $EuCd_2Sb_2$, Physical Review B **102**, 014408 (2020).

[24] N. F. Kharchenko, V. V. Eremenko, and O. P. Tutakina, Light birefringence bilinear in the ferromagnetic and antiferromagnetic vectors in cobalt carbonate, ZhETF Pisma Redaktsiiu **27**, 466 (1978).

[25] N. F. Kharchenko, V. V. Eremenko, and L. I. Belyĭ, Lowering of the optical class of an antiferromagnetic crystal, induced by a longitudinal magnetic field, ZhETF Pisma Redaktsiiu **28**, 351 (1978).

[26] N. Kharchenko and S. Gnatchenko, Linear Magneto-Optic Effect and Visual Observation of Anti-

Ferromagnetic Domains in Orthorhombic $DyFeO_3$ Crystal, Fizika Nizkikh Temperatur **7**, 475 (1981).
[27] V. Eremenko, S. Gnatchenko, N. Kharchenko, S. Sofroneev, J. Desvignes, P. Feldmann, and H. Legall, Linear Magneto-Optic Effect in Tetragonal Antiferromagnetic Garnet $Ca_3Mn_2Ge_3O_{12}$, Acta Physica Polonica A **68**, 419 (1985).
[28] V. V. Eremenko and N. F. Kharchenko, Magneto-optics of antiferromagnets, Physics Reports **155**, 379 (1987).
[29] V. V. Eremenko, N. F. Kharchenko, L. I. Beliy, and O. P. Tutakina, Birefringence of the antiferromagnetic crystals linear in a magnetic field, Journal of Magnetism and Magnetic Materials **15–18**, 791 (1980).
[30] V. V. Eremenko, Y. G. Litvinenko, N. K. Kharchenko, and V. M. Naumenko, Magneto-Optical Methods for Investigating the Structure of Antiferromagnetically Ordered Crystals, in *Magneto-Optics and Spectroscopy of Antiferromagnets*, edited by V. V. Eremenko, Y. G. Litvinenko, N. K. Kharchenko, and V. M. Naumenko (Springer, New York, NY, 1992) pp. 67–110.
[31] N. F. Kharchenko, The linear magneto-optic effect as a manifestation of a higher order magnetoelectric effect, Ferroelectrics **162**, 173 (1994).
[32] C. Lee, P. Vir, K. Manna, C. Shekhar, J. E. Moore, M. A. Kastner, C. Felser, and J. Orenstein, Observation of a phase transition within the domain walls of ferromagnetic $Co_3Sn_2S_2$, Nature Communications **13**, 3000 (2022).
[33] I. Dzyaloshinsky, A thermodynamic theory of "weak" ferromagnetism of antiferromagnetics, Journal of Physics and Chemistry of Solids **4**, 241 (1958).
[34] R. Skomski, P. Manchanda, and A. Kashyap, Anisotropy and Crystal Field, in *Handbook of Magnetism and Magnetic Materials*, edited by M. Coey and S. Parkin (Springer International Publishing, Cham, 2021) pp. 1–83.
[35] Y. Ōnuki, M. Hedo, and F. Honda, Unique Electronic States of Eu-based Compounds, Journal of the Physical Society of Japan **89**, 102001 (2020).
[36] M. Colarieti-Tosti, S. I. Simak, R. Ahuja, L. Nordström, O. Eriksson, D. Åberg, S. Edvardsson, and M. S. S. Brooks, Origin of Magnetic Anisotropy of Gd Metal, Physical Review Letters **91**, 157201 (2003).
[37] S. Abdelouahed and M. Alouani, Magnetic anisotropy in Gd, GdN, and $GdFe_2$ tuned by the energy of gadolinium 4f states, Physical Review B **79**, 054406 (2009).
[38] M. Blanco-Rey, R. Castrillo-Bodero, K. Ali, P. Gargiani, F. Bertran, P. M. Sheverdyaeva, J. E. Ortega, L. Fernandez, and F. Schiller, Effect of the valence state on the band magnetocrystalline anisotropy in two-dimensional rare-earth/noble-metal compounds, Physical Review Research **4**, 013237 (2022).
[39] C. C. Homes, Z.-C. Wang, K. Fruhling, and F. Tafti, Optical properties and carrier localization in the layered phosphide $EuCd_2P_2$, Physical Review B **107**, 045106 (2023).
[40] C. Timm, M. E. Raikh, and F. von Oppen, Disorder-Induced Resistive Anomaly Near Ferromagnetic Phase Transitions, Physical Review Letters **94**, 036602 (2005).
[41] Z. Wang, K. Barros, G.-W. Chern, D. L. Maslov, and C. D. Batista, Resistivity Minimum in Highly Frustrated Itinerant Magnets, Physical Review Letters **117**, 206601 (2016).
[42] B. Flebus, Magnetoresistance driven by the magnetic Berezinskii-Kosterlitz-Thouless transition, Physical Review B **104**, L020408 (2021).
[43] E. Heinrich, T. Posske, and B. Flebus, Topological magnetic phase transition in Eu-based A-type antiferromagnets (2022), arXiv:2207.02361 [cond-mat].
[44] M. Pohlit, S. Rößler, Y. Ohno, H. Ohno, S. von Molnár, Z. Fisk, J. Müller, and S. Wirth, Evidence for Ferromagnetic Clusters in the EuB_6, Physical Review Letters **120**, 257201 (2018).
[45] P. Das, A. Amyan, J. Brandenburg, J. Müller, P. Xiong, S. von Molnár, and Z. Fisk, Magnetically driven electronic phase separation in the semimetallic ferromagnet EuB_6, Physical Review B **86**, 184425 (2012).
[46] M. L. Brooks, T. Lancaster, S. J. Blundell, W. Hayes, F. L. Pratt, and Z. Fisk, Magnetic phase separation in EuB_6 detected by muon spin rotation, Physical Review B **70**, 020401 (2004).